Original Article

MICROSTRUCTURAL MORPHOLOGY AND MECHANICAL ANALYSIS OF DECELLULARIZED LIGAMENT SCAFFOLDS

J.L. Sun[1], M.Y. Yang[1], J.H. Zhou[1], N. Jiang[1,*] and H.Z. Chen[1,*]

[1]State Key Laboratory of Oral Diseases & National Center for Stomatology & National Clinical Research Center for Oral Diseases, West China Hospital of Stomatology, Sichuan University, 610041 Chengdu, Sichuan, China

Abstract

Background: The limited self-repair capacity of ligaments imposes substantial obstacles to effective tissues healing, thereby highlighting decellularization as a viable approach for ligament reconstruction. While whole tissue decellularization retains gross morphological features, its impact on microstructural organization and multiscale mechanical behavior remains insufficiently elucidated. **Methods**: Rabbit medial collateral ligaments were decellularized using a combined protocol of physical, chemical, and biological methods, comprising five freeze-thaw cycles (physical), 0.38 g/mL guanidine and 0.5 % sodium dodecyl sulfate (SDS) (chemical), and 0.5 % trypsin (biological). Decellularization efficacy was validated through hematoxylin-eosin (HE) and 4′,6-diamidino-2-phenylindole (DAPI) staining and biochemical quantification of deoxyribonucleic acid (DNA), glycosaminoglycan (GAG), and collagen content. Structural and mechanical alterations across scales were assessed via scanning electron microscopy (SEM), fluorescence collagen hybridizing peptide (F-CHP) staining, atomic force microscopy (AFM), uniaxial tensile testing, and nanoindentation. Statistical analyses were performed using unpaired *t*-tests. **Results**: The decellularization process significantly reduced DNA content (from 1110.77 ± 46.16 ng/mg to 38.60 ± 1.67 ng/mg) and disrupted collagen organization, as reflected by a decreased tensile modulus (3.16 ± 0.19 MPa vs. 3.84 ± 0.23 MPa). Microscopic evaluations revealed structural alterations in collagen fibrils, including increased porosity and expanded D-banding periodicity. Nanoindentation and AFM results indicated a decrease in mechanical properties at micrometer and nanometer scales, with compromised energy dissipation capacity. Under extreme tensile conditions, decellularized ligaments demonstrated pronounced fiber tearing and misalignment. **Conclusions**: Decellularization induces hierarchical disorganization of ligaments matrix at both micrometer and nanometer scales, typified by collagen fiber loosening, augmented interfibrillar spacing, and expanded D-banding periodicity. These alterations collectively lead to impaired micromechanical integrity and reduced energy dissipation. The findings highlight critical structural determinants of mechanical function and provide insights for optimizing decellularization strategies to preserve microscopic architecture and meet the demands of load-bearing applications.

Keywords: Decellularization, microstructural morphology, mechanical behavior, microscopic analysis, ligaments.

***Address for correspondence**: H.Z. Chen, State Key Laboratory of Oral Diseases & National Center for Stomatology & National Clinical Research Center for Oral Diseases, West China Hospital of Stomatology, Sichuan University, 610041 Chengdu, Sichuan, China. Email: drchenhz2018@163.com; N. Jiang, State Key Laboratory of Oral Diseases & National Center for Stomatology & National Clinical Research Center for Oral Diseases, West China Hospital of Stomatology, Sichuan University, 610041 Chengdu, Sichuan, China. Email: dent_jn@163.com.

Introduction

Ligaments, composed predominantly of collagen-rich connective tissue, serve as essential stabilizing components within joints [1,2]. Their primary mechanical functions include force transmission, shock absorption, energy storage and release, stress dispersion, and the maintenance of joint stability and coordinated kinematics [3,4]. These biomechanical roles are critical for protecting the structural integrity and functional synergy of muscles, bones, and joint elements [5]. The integrity of ligaments with other joint structures, is vital for sustaining physiological mobility and minimizing the risk of sports-related injuries [6,7].

Ligament damage can arise from acute trauma, aging and degeneration, overuse, or biomechanical misalignment, often resulting in pain, swelling, altered load distribution, and musculoskeletal imbalance [8,9]. In severe cases, such injuries may progress to functional deficits, post-traumatic osteoarthritis, and long-term quality-of-life impairment [10–12]. The intrinsic challenges of ligament healing—attributable to limited vascularization, in-

tricate hierarchical architecture, and sluggish regenerative capacity—frequently necessitate surgical intervention for tissue repair or replacement in cases of substantial damage [13–15].

The advent of biomaterial scaffolds has introduced promising avenues for ligament repair, with decellularized scaffolds emerging as particularly compelling candidates [16,17]. Decellularization techniques involve removing cellular components from tissues through physical, chemical, and biological methods to prevent immune rejection while preserving the extracellular matrix to form scaffolds that facilitate cell adhesion, proliferation, differentiation, and ultimately tissue repair and regeneration [18,19].

Whole tissue decellularization, which maintains the native three-dimensional morphology of the tissue, offers advantages for structural integration in repair and reconstruction contexts [20,21]. Nevertheless, preliminary evidence suggests that this approach may compromise tissue mechanical integrity [22,23], posing limitations for *in vivo* applications where mechanical resilience is paramount [24]. Although gross morphology remains intact, we hypothesize that changes in the microstructure lead to alterations in micro-mechanical properties, ultimately affecting the macroscopic mechanical properties of the tissue after decellularization.

Table 1 (Ref. [25–29]) summarizes the current applications of whole tissue decellularization in ligaments, alongside its reported effects on mechanical properties. Prior investigations have predominantly emphasized macroscopic outcomes, such as tissue morphology and bulk mechanical strength while neglecting microscale evaluations. The present study addresses this gap by examining microstructural and micromechanical alterations induced by decellularization. Through comprehensive analysis of ligament morphology and mechanical characteristics before and after decellularization, the study elucidates the structural and functional repercussions at the microscopic level. Additionally, the effects of tensile deformation under both physiological and extreme loading conditions on collagen fiber architecture were assessed. This insight could also offer new perspectives and ideas for restoring the microstructural morphology and mechanical properties of tissues post-treatment.

Materials and Methods

Decellularization Protocol for the Medial Collateral Ligament of Rabbit Knee Joint

The decellularization protocol was adapted and optimized based on established methodologies [24,30,31]. Under sterile conditions, the medial collateral ligaments of the knee joints were harvested from healthy male New Zealand white rabbits (4 months old, weighing 1.9–2.1 kg). The ligament tissues were pretreated by repeated freeze-thaw cycles under –20 °C and 4 °C conditions for a total of 5 cycles, with each freeze and thaw phase lasting 12 h. The pretreated ligaments were incubated at 4 °C in a guanidine solution (biofroxx, Batch No. EZ6387417F; Einhausen, Germany) with a concentration of 0.38 g/mL for 48 h. Subsequently, they were treated at 37 °C in a 0.5 % trypsin solution (Gibco, Batch No. 15400054; Grand Island, NY, USA) for 24 h. Finally, the ligaments were processed at room temperature in a 0.5 % sodium dodecyl sulfate (SDS) solution (biofroxx, Batch No. EZ6408AB7C; Einhausen, Germany) for 24 h, resulting in decellularized rabbit ligament tissues.

Histological Analysis

Fresh and decellularized rabbit ligament tissues (for each group, n = 3) were fixed in 4 % paraformaldehyde solution and rinsed thoroughly under running water. Samples were then dehydrated using an automated tissue dehydrator (Leica, Version No. ASP300S; Wetzlar, Germany) and embedded in paraffin. Sections with a thickness of 5 μm were cut along the longitudinal axis of the ligament and stained with hematoxylin-eosin (HE) and 4′,6-diamidino-2-phenylindole (DAPI) to evaluate the effectiveness of the decellularization process. Fast Green staining was used to observe the collagen distribution.

For HE staining, tissue sections were processed using a commercial HE staining kit (Solarbio, Batch No. G1120; Beijing, China). Sections were stained with hematoxylin solution for 5 minutes, rinsed with water, and subsequently counterstained with eosin solution for 1 minute. For DAPI staining, sections were incubated with DAPI solution from a staining kit (Solarbio, Batch No. C0065; Beijing, China) for 5 minutes in the dark, followed by gentle washing with phosphate buffered saline (PBS). For Fast Green staining, sections were stained using a Fast Green staining kit (Solarbio, Batch No. G1371; Beijing, China) for 5 minutes, then rinsed to remove excess dye before imaging.

Fluorescein collagen hybridizing peptide (F-CHP) staining: The prepared CHP staining solution (1:7, 3Helix, Batch No. FLU300; Salt Lake City, UT, USA) was heated in an 80 °C water bath for 5 minutes and then rapidly cooled on ice to room temperature. The CHP staining solution was then applied to tissue sections and incubated overnight at 4 °C. Following incubation, the sections were thoroughly washed with PBS. The degree of collagen denaturation in the tissue was observed using a fluorescence microscope.

Immunofluorescence staining: Tissue sections were subjected to antigen retrieval using Tris-ethylenediaminetetraacetic acid (EDTA) buffer. Then the sections were blocked with 5 % goat serum at room temperature for 30 minutes. Primary antibodies were applied individually, including collagen I (COL-1, 1:300, Servicebio, Batch No. GB11022; Wuhan, China), collagen III (COL-3, 1:300, Servicebio, Batch No. GB111629; Wuhan, China), and fibronectin (1:200, Abcam, Batch No. ab268020; Waltham, MA, USA). Sections were incubated overnight at 4 °C, followed by thorough washing. Subsequently, species-specific secondary antibodies

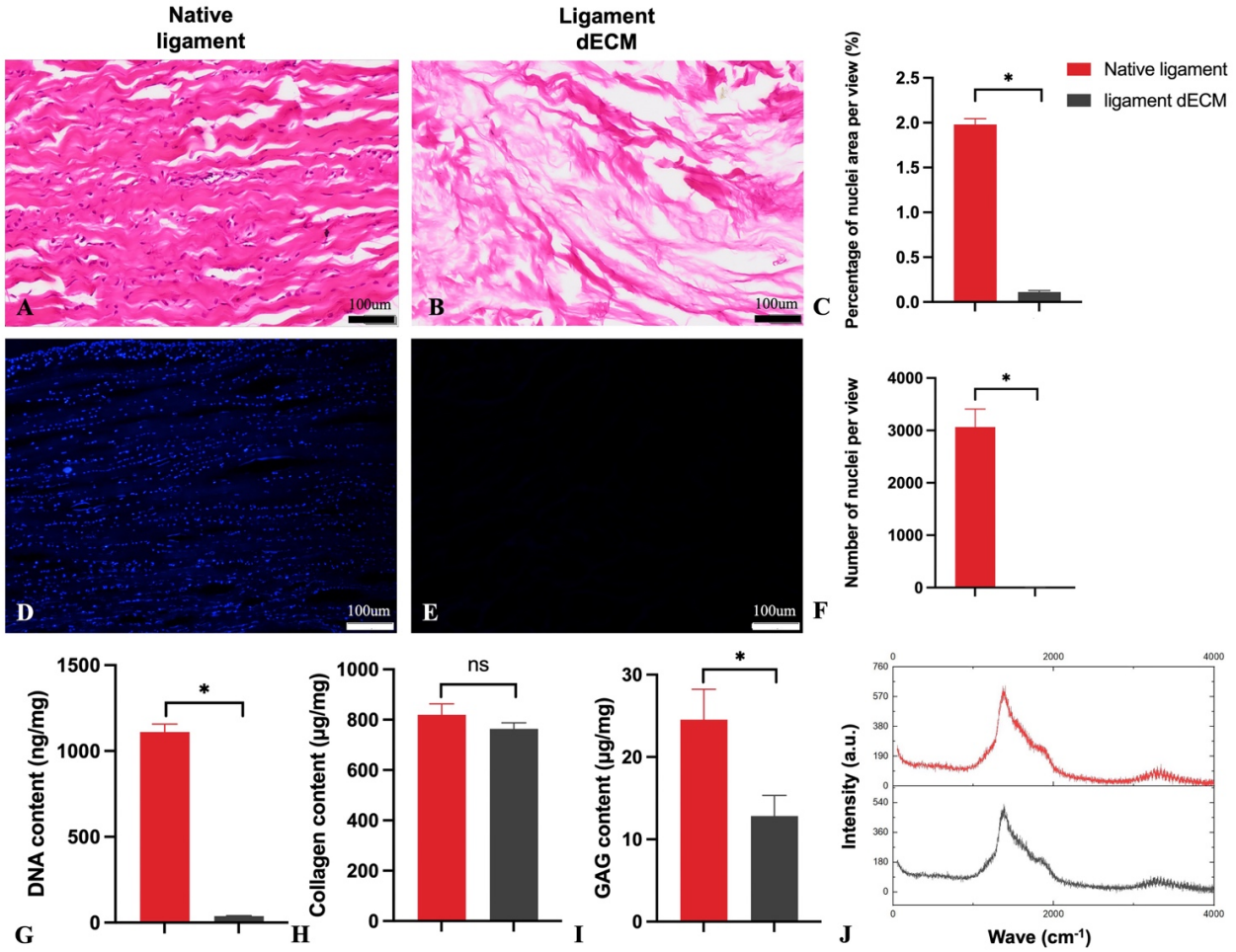

Fig. 1. Validation of the decellularization effect in rabbit ligament tissue. (**A,B**) HE staining of native ligament and ligament decellularized extracellular matrix (dECM). Scale bar: 100 μm. (**C**) Quantification results of HE staining. (**D,E**) DAPI staining of native ligament and ligament dECM. Scale bar: 100 μm. (**F**) Quantification results of DAPI staining. (**G**) DNA content quantification. (**H**) Collagen content quantification. (**I**) GAG content quantification. (**J**) Raman spectroscopy results of native ligament and ligament dECM. HE, hematoxylin-eosin; DAPI, 4′,6-diamidino-2-phenylindole; DNA, deoxyribonucleic acid; GAG, glycosaminoglycan; $^{*}p < 0.05$; ns, $p > 0.05$. This image was produced using GraphPad Prism and Origin software.

corresponding to the primary antibodies were added and incubated at room temperature for 50 minutes. After washing, fluorescence signals were observed using a fluorescence microscope (Olympus FV3000; Tokyo, Japan).

Biochemical Composition Analysis

Deoxyribonucleic acid (DNA) quantification: Fresh and decellularized rabbit ligament tissues (for each group, n = 4) were freeze-dried and weighed to determine the dry weight. Each sample was enzymatically digested using a proteinase K solution (1 mg/mL, biofroxx, Batch No. 1124MG100; Einhausen, Germany) proportionally prepared according to tissue weight, followed by incubation at 56 °C in a water bath overnight to ensure complete digestion. DNA content was then quantified using the PicoGreen DNA assay kit (Thermo Fisher, Batch No. 2544406; Waltham, MA, USA) according to the manufacturer's instructions.

Glycosaminoglycan (GAG) quantification: After complete digestion with proteinase K, the solutions of the two groups of tissue were separately mixed with prepared dimethylmethylene blue (DMMB) solution. The GAG contents of the two groups (for each group, n = 4) were calculated by measuring the wavelength of 535 nm using a microplate reader (Thermo Fisher, Varioskan LUX, Batch No. 3020-1134; Waltham, MA, USA).

Collagen quantification: Hydroxyproline (HYP) was selected as a marker for the total collagen content in the tissue. The absorbances of the two sample groups (for each group, n = 4) were measured at a wavelength of 570 nm. The collagen content was calculated based on that HYP constitutes approximately 13.5 % of the total collagen.

Table 1. Published studies of decellularized ligament/tendon with hierarchical mechanical characteristic and microstructural morphology.

Decellularized tissue	Fabrication method	Macro-mechanical properties	Microstructural morphology	Micro-mechanical properties	Changes in physiological or overloading states	Reference
Human PIP joint collateral ligaments	0.1 % EDTA and 0.1 % SDS for 24 h, 5 % PAA for 6 h	Decellularized ligaments revealed lower displacement to failure compared with untreated ligaments	NA	NA	NA	[25]
Rabbit patella ligament	Aponeurosis discission and decellularization: 0.05 % trypsin for 5 h and 1 % Triton X-100 for 48 h	There were no significant differences in the maximum load at rupture and elastic modulus of the native tissue compared with decellularized tissue	After decellularization, the interspaces between the collagen fibers had significantly increased	NA	NA	[26]
Porcine and human anterior cruciate ligaments	Freeze-thawed five times, 1 % Triton X-100 for 24 h to solubilize membrane proteins, and Benzonase for 24 h to degrade DNA and RNA. Then 1 % Triton X-100 for 72 h and Benzonase for 48 h.	For porcine samples, the stiffness in the linear region decreases after decellularization	Collagen fibers in human native ACLs are thinner and more tightly packed than those in decellularized ACLs	NA	NA	[27]
Porcine anterior cruciate ligaments	Six times freeze-thaw cycles, 0.5 % trypsin for 6 h, 2 % Triton X-100 for 3 d, and 50 U mL^{-1} deoxyribonuclease for 2 d	There is no comparison of mechanical properties between decellularized tissue, bioink and native tissue. The mechanical properties improved after subcutaneous implantation in nude mice	The result of SEM shows that LidECM has a contiguous collagenous network with oriented fiber bundles which resemble native ligament	NA	NA	[28]
Rabbit hamstring tendon	0.05 % trypsin-EDTA for 1 h, 1.5 % PAA and 2.0 % Triton X-100 for 4 h, and different neutralizing reagents for 8 h	No comparison between native and decellularized tissues	Decellularized allografts neutralized by 5 % calcium bicarbonate had typical reticular and porous microstructures with optical cytocompatibility	NA	NA	[29]

EDTA, ethylenediaminetetraacetic acid; SDS, sodium dodecyl sulfate; PAA, peracetic acid; DNA, deoxyribonucleic acid; RNA, ribonucleic acid; NA, not available; ACL, anterior cruciate ligament; LidECM, ligament-derived decellularized extracellular matrix; SEM, scanning electron microscopy; PIP, proximal interphalangeal.

European Cells and Materials Vol.53 2025 (pages 28–40) DOI: 10.22203/eCM.v053a03

Raman Spectroscopy Analysis

Fresh and decellularized rabbit ligament tissues (for each group, n = 3) were embedded in optimal cutting temperature (OCT) compound (SAKURA, Batch No. 5331-00; Torrance, CA, USA) and cryosectioned longitudinally into 100 μm slices. Following PBS washing to remove residual OCT, Raman spectra were obtained using a Raman microscope (Renishaw InVia, Batch No. 54VQ49; Gloucestershire, UK) with a 785 nm excitation source. The spectra were collected within the range of 50–4000 cm^{-1}.

Scanning Electron Microscopy (SEM) Observation

Ligament tissue samples from different treatment groups (for each group, n = 3) were sectioned longitudinally and fixed in 2.5 % glutaraldehyde solution at 4 °C. After washing with PBS, the tissues were dehydrated in a graded ethanol series with concentrations of 50 %, 75 %, 80 %, 90 %, 95 %, and 100 %. The samples were then subjected to critical point drying, and the observation surface was placed facing upward on the specimen holder, followed by gold sputter coating. The cross-sectional structures of the tissues before and after decellularization were observed by scanning electron microscopy (SEM, Helios, Batch No. 4421-001308, originally by Field Electron and Ion (FEI) Company, now Thermo Fisher, Waltham, MA, USA) at different magnifications.

Uniaxial Tensile Mechanical Testing and Sample Preparation under Different Strain Conditions

For mechanical characterization, ligament samples (for each group, n = 3) were equilibrated in PBS to ensure consistent hydration. The testing direction was set along the longitudinal axis of the ligament, with a stretching speed of 5 mm/min. The tests were conducted on a mechanical testing machine (Lixian Instrument Technology Co., Batch No. HZ-1004A; Dongguan, China). The dimensions of the testing area (length, width, and thickness) were measured, and load-displacement data generated during the tests were converted to stress-strain curves using Origin software (OriginLab, version2021; Northampton, MA, USA). The slope of the curve within the 5 %–20 % strain range was calculated as the elastic modulus. Additionally, in this study, 5 % strain was set to simulate physiological conditions, while 30 % strain was used to simulate extreme conditions [32,33]. After stretching to different strain levels, the microstructural features of the samples were observed under SEM.

Nanoindentation Testing

Fresh and decellularized ligament tissues (for each group, n = 3) were placed on the stage of a nanoindenter (Piuma, Batch No. Optics11-20194162; Amsterdam, Netherlands), with all testing conducted in an aqueous environment. A nano-indentation probe with a tip radius of 9 μm and an elastic constant of 5 N/m was used for testing. The load-displacement curves during loading and unloading were recorded, and the slope of the 20 %–90 % segment of the unloading curve was calculated as the elastic modulus using the power-law fitting of the Hertz model. The energy dissipation capacity was determined by measuring the area enclosed by the loading and unloading curves. The area between the loading and unloading curves was denoted as E1, and the area beneath the unloading curve was denoted as E2. The energy dissipation ratio was calculated as E1/(E1 + E2) [34,35].

Atomic Force Microscopy (AFM) Testing

Rabbit ligament tissues from different groups (for each group, n = 3) were embedded in OCT, ensuring that the embedding direction aligned with the scanning electron microscopy observation direction. Cryosectioning was performed using a cryostat (Leica, Version No. CM1950; Wetzlar, Germany) to obtain longitudinal slices of 40 μm thickness. The prepared samples were placed on the sample stage of the scanning probe microscope (SPM) instrument (Shimadzu, Version No. SPM-9600; Kyoto, Japan). In dynamic mode, the morphological structure of the target area was observed at a frequency of 1 Hz and a resolution of 512 × 512 pixels. For mechanical property testing, a contact-mode silicon probe with gold coating (CSG) 10 probe was used in contact mode at a frequency of 6 Hz and a resolution of 64 × 64 pixels. Data were analyzed using Nano 3D Mapping Fast software (Shimadzu, Version No. 6.0.4; Kyoto, Japan), and the JKR model was applied to calculate the elastic modulus.

Residue SDS Quantification

According to the instructions of the Residual SDS Assay Kit (Sangon Biotech, Batch No. C500055-0100; Shanghai, China), reagents were added to the solutions from both groups (for each group, n = 3) and mixed thoroughly. The mixtures were then centrifuged at 5000 rpm for 5 minutes. The supernatants were collected, and absorbance was measured at 499 nm to calculate the residual SDS content in each sample.

Biocompatibility Evaluation

Under sterile conditions, femurs were harvested from healthy male New Zealand rabbits (4 months old, weighing 1.9–2.1 kg), and the epiphyses at both ends were removed. The bone marrow cavity was repeatedly flushed with PBS containing 5 % penicillin-streptomycin to collect bone marrow cells. The resulting cell suspension was centrifuged at 1500 rpm for 5 minutes, the supernatant was discarded, and the pellet was resuspended in growth medium (Gibco, Batch No. 6125188; Grand Island, NY, USA). Cells were seeded into culture flasks and maintained in an incubator at 37 °C with 5 % CO_2. The cells were mycoplasma-free (polymerase chain reaction (PCR) Mycoplasma Test Kit, absin, Batch No. 322A036; Shanghai, China). Third-passage cells were then seeded onto scaffolds from different

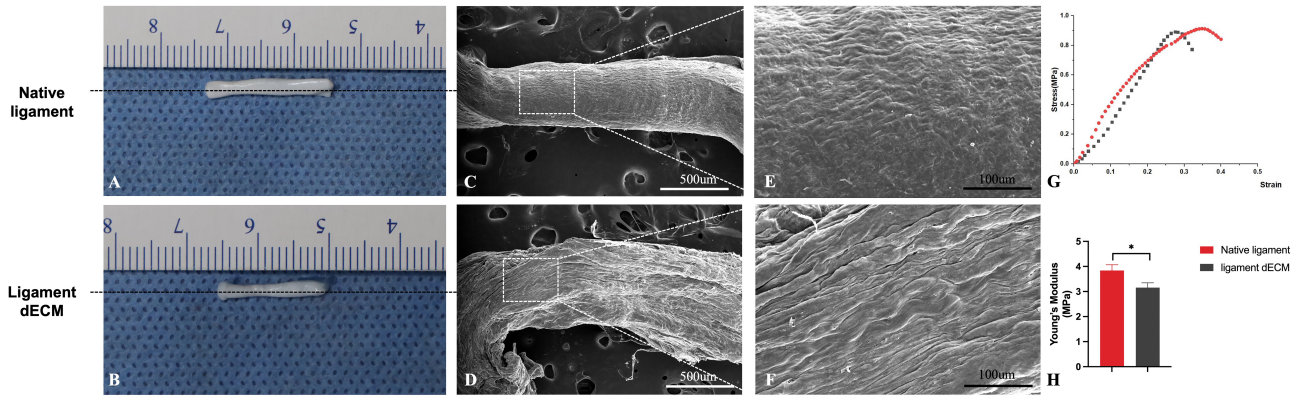

Fig. 2. Analysis of macro and sub-macro characteristics. (**A,B**) Gross morphology of native ligament and ligament dECM. (**C,D**) SEM images of native ligament and ligament dECM at 200× magnification. Scale bar: 500 μm. (**E,F**) SEM images of native ligament and ligament dECM at 1000× magnification. Scale bar: 100 μm. (**G**) Stress-strain curves of uniaxial tensile mechanical testing. (**H**) Quantitative results of Young's modulus. SEM, scanning electron microscopy; $^{*}p < 0.05$. This image was produced using Adobe Illustrator, GraphPad Prism and Origin software.

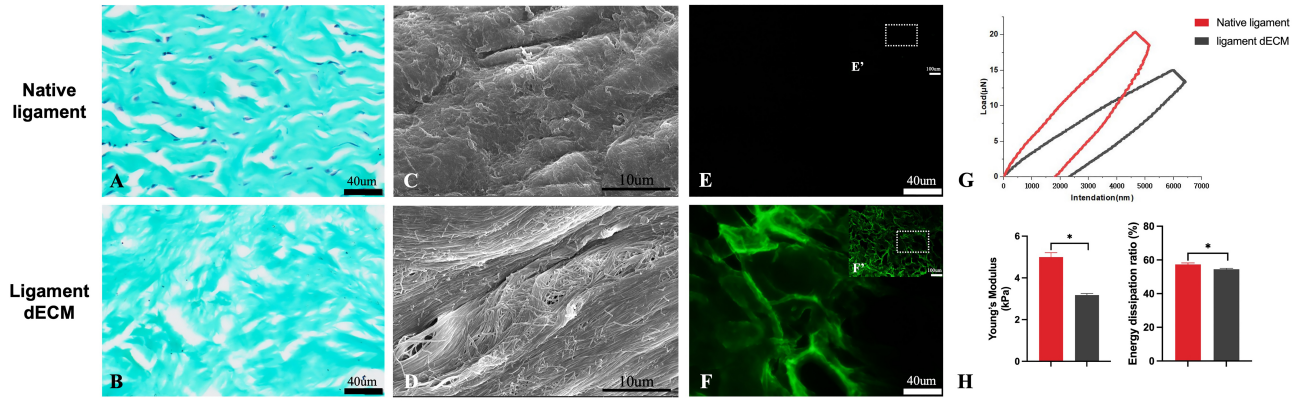

Fig. 3. Microscopic analysis at the micrometer scale. (**A,B**) Fast Green staining of native ligament and ligament dECM. Scale bar: 40 μm. (**C,D**) SEM images of native ligament and ligament dECM at 10,000× magnification. Scale bar: 10 μm. (**E,F**) Enlarged area of F-CHP staining of native ligament and ligament dECM. Scale bar: 40 μm. (**E',F'**) F-CHP staining of native ligament and ligament dECM. Scale bar: 100 μm. (**G**) Load-intendation curves of nanoindentation testing. (**H**) Quantitative results of Young's modulus and energy dissipation ratio. F-CHP, fluorescence collagen hybridizing peptide; $^{*}p < 0.05$. This image was produced using Adobe Illustrator, GraphPad Prism and Origin software.

experimental groups (for each group, n = 3) for subsequent experiments.

Cell proliferation on days 1, 3, 5, and 7 was evaluated using the Cell Counting Kit-8 (CCK-8, APExBIO, Batch No. 25004K1018; Houston, TX, USA) in accordance with the manufacturer's protocol. Absorbance was measured at 450 nm, and the average optical density (OD) was calculated from four replicate wells.

Cell viability on the sample surfaces was assessed using a Live/Dead assay kit (Yobibio, Batch No. U23-002A; Shanghai, China). Briefly, 1 mL of calcein-acetoxymethyl ester (AM)/propidium iodide (PI) staining solution was added to each well of a 24-well plate, followed by incubation at 37 °C for 30 minutes. The samples were then rinsed three times with PBS, and cells were observed and counted under a confocal microscopy. On day 7, cell viability was quantified as the percentage of live cells relative to the total number of cells.

Statistical Analysis

All experiments were conducted with at least three replicate samples per group. Data are presented as mean ± standard deviation (SD). Statistical differences were analyzed using an unpaired *t*-test in GraphPad Prism 9 (GraphPad Software, San Diego, CA, USA), with significance defined at $p < 0.05$.

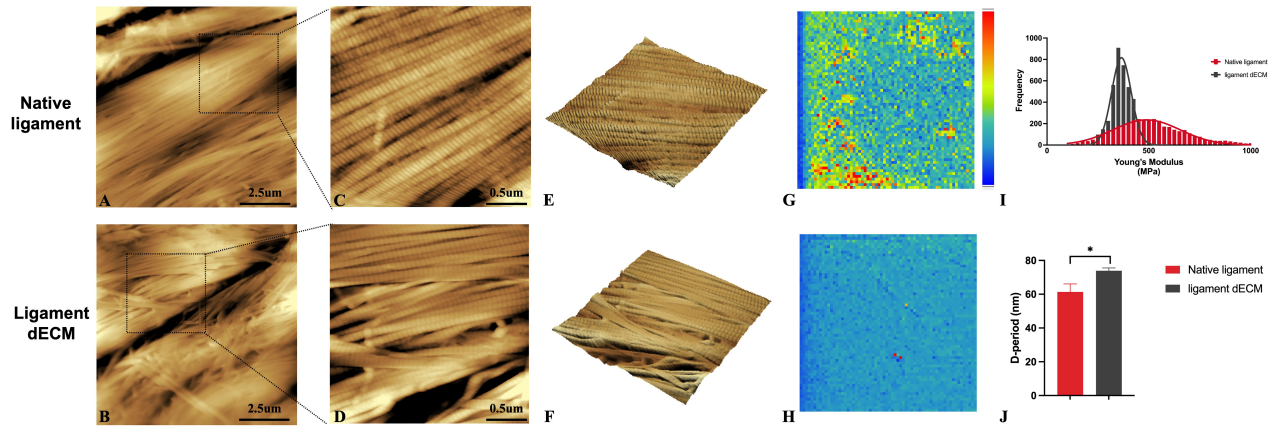

Fig. 4. Microscopic analysis at the nanometer scale. (**A-D**) AFM images of native ligament and ligament dECM. Scale bar in **A** and **B**: 2.5 μm. Scale bar in **C** and **D**: 0.5 μm. (**E,F**) Three-dimensional reconstruction of the Fig. 4**C,D**. (**G,H**) The AFM images of Young's modulus mapping of native ligament and ligament dECM. (**I**) Distribution of Young's modulus of native ligament and ligament dECM. (**J**) Quantitative results of D-period length. AFM, atomic force microscopy; $^{*}p < 0.05$. This image was produced using SPM-Nanoa, GraphPad Prism and Origin software.

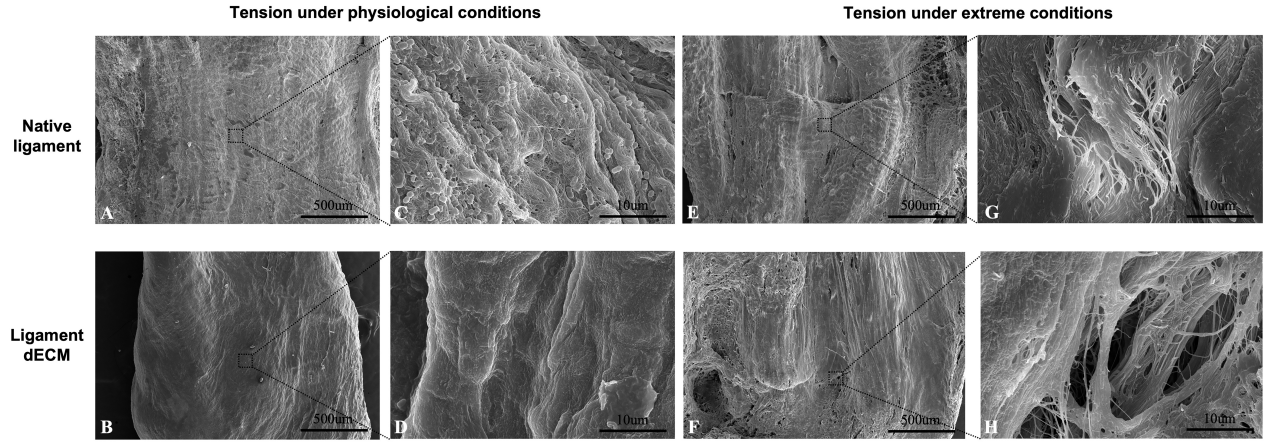

Fig. 5. The microscopic characteristics of ligament tissue before and after decellularization under different tensile conditions. (**A,B**) SEM images of native ligament and ligament dECM after tension motion under physiological conditions at 200× magnification. Scale bar: 500 μm. (**C,D**) SEM images of native ligament and ligament dECM after tension motion under physiological conditions at 10,000× magnification. Scale bar: 10 μm. (**E,F**) SEM images of native ligament and ligament dECM after tension motion under extreme conditions at 200× magnification. Scale bar: 500 μm. (**G,H**) SEM images of native ligament and ligament dECM after tension motion under extreme conditions at 10,000× magnification. Scale bar: 10 μm. This image was produced using Adobe Illustrator software.

Results

Validation of the Decellularization Effect in Rabbit Ligament Tissue

HE staining and quantification results (Fig. 1**A–C**) demonstrated that, in cross-sections of native rabbit medial collateral ligament, cells were uniformly distributed within the collagen fibers, with basophilic-stained nuclei appearing distinctly purple-blue and sharply defined. The extracellular matrix was densely organized and structurally continuous. Following application of the combined decellularization protocol—comprising five freeze-thaw cycles (physical), 0.38 g/mL guanidine and 0.5 % SDS (chemical), and 0.5 % trypsin (biological)—cell nuclei were entirely absent, and the matrix displayed a markedly looser arrangement. DAPI staining and quantification results (Fig. 1**D-F**) corroborated these findings, indicating dense nuclear distribution in native tissue and a complete absence of nuclear material post-decellularization. Biochemical content analysis revealed that the DNA content in the ligaments decreased significantly from 1110.77 ± 46.16 ng/mg to 38.60 ± 1.67 ng/mg (Fig. 1**G**). Collagen content remained stable, with no statistically significant difference observed before and after decellularization ($p = 0.07$) (Fig. 1**H**). GAG content in the rabbit medial collateral ligament constitutes a relatively small proportion of the tissue's dry weight, approximately 24.55 ± 3.68 μg/mg. The decellularization process

induced a substantial depletion of GAG content, resulting in a reduced concentration of 12.83 ± 2.5 μg/mg (Fig. 1**I**). The Raman results (Fig. 1**J**) indicated that although decellularization led to a reduction in the intensity of the ligament spectra to some extent, characteristic peaks, including amide I and methylene/methyl groups (CH_2/CH_3), were preserved. Residual SDS quantification was performed to assess the potential presence of remaining decellularization agents. The results showed that the SDS content in the decellularized extracellular matrix (dECM) group was nearly undetectable and comparable to that of the native ligament group, indicating effective removal of SDS through the post-decellularization washing processes. Cell proliferation was assessed using the CCK-8 assay on days 1, 3, 5, and 7 (**Supplementary Fig. 1A**). Compared with the control group, cells cultured on the decellularized scaffold exhibited a significant increase in absorbance from day 5 onwards ($p < 0.0001$), indicating enhanced cell proliferation on the scaffold surface. To further evaluate cell viability, Live/Dead staining was performed on day 7. As shown in **Supplementary Fig. 1B**, the majority of cells displayed intense green fluorescence (live), with only a few red-stained (dead) cells observed. Quantitative analysis (**Supplementary Fig. 1C**) revealed a high percentage of live cells (99.75 %), demonstrating excellent biocompatibility of the decellularized ligament scaffold. Immunofluorescence staining for Collagen I, Collagen III, and fibronectin was performed on native and decellularized ligament tissue sections. As shown in **Supplementary Fig. 2A–F**, positive immunofluorescence signals for all three extracellular matrix (ECM) proteins were observed in both groups. Quantitative analysis of relative fluorescence intensity (**Supplementary Fig. 2G**) showed no statistically significant differences between the two groups ($p > 0.05$).

Analysis of Macro and Sub-Macro Characteristics

The decellularization protocol used in this study did not include preprocessing steps such as grinding or homogenization, thereby preserving the gross morphology of the tissue. The decellularized ligament retained a structural appearance closely resembling that of native tissue, exhibiting no visible perforation, fragmentation, or other structural damage (Fig. 2**A,B**). SEM revealed no appreciable differences in tissue architecture at low magnification (Fig. 2**C,D**). However, high-magnification imaging exposed distinct ultrastructural changes: collagen fibers in native ligaments appeared densely packed with minimal interstitial space (Fig. 2**E**), whereas post-decellularization tissues exhibited increased porosity, looser fiber organization, and more prominent undulations (Fig. 2**F**). Macroscopic tensile mechanical testing of the ligament tissue (Fig. 2**G,H**) revealed that the Young's modulus of the decellularized ligament was 3.16 ± 0.19 MPa, which was significantly lower than that of the native ligament (3.84 ± 0.23 MPa) ($p = 0.02$). This mechanical decline is likely attributable to alterations in the internal architecture induced by the decellularization agents, despite the preservation of external three-dimensional morphology. Subsequent analysis focused on micro- and nanoscale changes in the ligament before and after decellularization, aiming to elucidate the underlying mechanisms of mechanical compromise.

Microscopic Analysis at the Micrometer Scale

Fast Green staining (Fig. 3**A,B**) revealed that tightly arranged collagen fibers in the native ligament tissue were interspersed with nuclei, which were completely absent after decellularization. While the collagen fibers did not exhibit any fractures post-decellularization, they became noticeably looser compared with the pre-treatment state. High-magnification SEM (Fig. 3**C,D**) further confirmed that decellularization induced micron-scale porosity in the previously dense and compact collagen fiber network of the ligament tissue. Additionally, the fine collagen fiber bundles became more distinguishable after the treatment. The F-CHP staining results revealed that (Fig. 3**E,F,E',F'**), compared with the absence of fluorescence signals in native tissue, distinct enhanced green fluorescence was observed in the decellularized tissue. This indicates that the decellularization process induced collagen helix unwinding in the ligament tissue, leading to collagen fiber denaturation and modification. Nanoindentation results (Fig. 3**G,H**) revealed that the modulus of collagen fibers after decellularization (3.18 ± 0.08 kPa) was significantly reduced compared with that of collagen fibers in native ligaments (5.00 ± 0.21 kPa) ($p = 0.0001$). This finding demonstrates that the alterations in the micro-scale morphological structure indeed led to a reduction in the mechanical properties of collagen fibers at the micron scale.

Microscopic Analysis at the Nanometer Scale

High-resolution AFM offers a detailed and multidimensional evaluation of the microstructural and micromechanical alterations resulting from decellularization. The results (Fig. 4**A–F**) revealed that in native ligament tissue, collagen fibrils were arranged in a well-organized "corn-like" architecture, characterized by tightly packed alignment and a consistent D-banding periodicity, with no discernible inter-fibrillar gaps. After decellularization, noticeable increases in the spacing between collagen fibrils within the extracellular matrix were observed. The characteristic distribution of the D-banding periodicity became less distinct compared with the native tissue. Mechanical mapping images (Fig. 4**G,H**) and quantitative results (Fig. 4**I**) from AFM demonstrated a significant reduction in the modulus distribution range of collagen fibrils in decellularized tissues relative to native counterparts, indicating compromised mechanical integrity. The D-banding periodicity itself was found to increase (Fig. 4**J**). The changes in D-band periodicity observed in this study may be a key factor contributing to the altered mechanical properties of collagen

fibrils following decellularization. Future research on ligament tissue repair should focus on the reconstruction of the D-band, aiming to restore the highly ordered periodic arrangement of collagen molecules.

The Microscopic Characteristics of Ligament Tissue before and after Decellularization under Different Tensile Conditions

SEM analysis under simulated physiological tensile conditions demonstrated that both pre- and post-decellularized ligament tissues maintained collagen fiber integrity during normal activity ranges, with no evident structural abnormalities found in collagen fibers (Fig. 5**A–D**). Microstructural images of ligament tissues before and after decellularization under extreme tensile conditions revealed that collagen fibers in the native ligament elongated and became taut, while collagen fibers in the decellularized ligament exhibited significant tearing, with the normal alignment of collagen fibers largely disrupted (Fig. 5**E–H**). These observations imply that decellularized scaffolds may lack the structural robustness required to endure excessive mechanical stress *in vivo*. This phenomenon aligns with our findings showing a reduction in the energy dissipation capacity of the decellularized ligament scaffold (Fig. 3**H**). The flow of interstitial fluid within the collagen network provides ligaments with their energy dissipation function. At the tissue level, water molecules within fibrils can rearrange during fibril deformation, generating reactive forces. However, the decellularization process alters the tissue structure, affecting the interstitial fluid and causing excessive fluid loss, which ultimately leads to a reduction in the ligament tissue's energy dissipation capacity. As one type of fibrous tissues that functions under load-bearing conditions, ligament repair and reconstruction should focus on whether it can meet the mechanical demands of *in vivo* activities, such as stretching.

Discussion

This study evaluates the impact of decellularization on the structural and mechanical properties of rabbit medial collateral ligament tissues across multiple scales. Utilizing an integrated physical, chemical, and biological decellularization protocol, the process markedly reduced the DNA content, validating its effectiveness in cellular component removal in accordance with internationally accepted decellularization benchmarks [36]. Subsequent analyses focused on the protocol's impact on the tissue's microstructure, mechanical behavior, and ability to withstand tensile loading under physiological and extreme conditions. While the overall morphology of the extracellular matrix remained intact, significant microstructural alterations—including increased collagen fiber porosity and disrupted D-banding periodicity—were identified. These modifications collectively contributed to a pronounced reduction in mechanical performance, notably in tensile modulus and energy dissipation capacity, underscoring the inherent challenges in preserving functional integrity within decellularized ligament scaffolds for *in vivo* use [37].

The observed loosening of collagen fibers and elevated porosity are likely attributable to the synergistic effects of the chemical (guanidine and SDS) and biological (trypsin) components of the decellularization protocol [38]. Specifically, SDS, as an ionic detergent, disrupts the structural stability of lipid membranes and induces protein denaturation by interfering with hydrophobic interactions, potentially compromising extracellular matrix integrity [39]. Additionally, SDS may impair collagen crosslinking by disrupting non-covalent interactions between collagen fibers, such as hydrophobic forces and hydrogen bonding, thereby facilitating a more disordered fiber architecture. Concurrently, trypsin, a serine protease, disrupts non-collagenous ECM proteins, such as fibronectin, which mediates adhesion between collagen fibers. This enzymatic degradation exacerbates fiber separation and compromises matrix cohesion [40].

F-CHP staining is a visualization technique used to detect collagen molecule damage [41]. It leverages engineered collagen hydrolyzing peptides that can specifically bind to unwound polypeptide chains of denatured collagen [42]. Damage to collagen partially unwinds its characteristic triple-helix structure, exposing the internal peptide chains [43]. F-CHP binds to these exposed peptide chains, thereby labeling the damaged collagen molecules. The fluorescence intensity corresponds to the degree and extent of damage [44]. This detection method offers higher sensitivity and accuracy, enabling the identification of even minor damage. Nanoindentation, characterized by its micron- to nanometer-scale spatial resolution, enables precise quantification of tissue micromechanical properties [45,46]. In this study, a nanoindentation instrument equipped with appropriately sized probes was utilized to assess the impact of decellularization on the mechanical properties of collagen fibers. Microscopic and nanoscopic analyses revealed that collagen fibers exhibited unwinding and denaturation, as evidenced by F-CHP staining and nanoindentation.

Under physiological tensile conditions, both native and decellularized ligaments preserved structural integrity. However, under excessive tensile strain, decellularized ligaments exhibited pronounced collagen fiber disruption and loss of alignment, indicative of diminished resistance to mechanical overload. These findings corroborate previous reports indicating that decellularization protocols can preserve tissue morphology while impacting mechanical properties [17,47]. Consistent with study on decellularized rabbit temporomandibular joint discs [24], the collagen content remained largely unchanged after decellularization, demonstrating the protocol's minimal impact on the proportion of collagen and its ability to maintain the structural framework of the extracellular matrix. Notably, this investigation provides additional insights at the micro-

and nanoscales, specifically the alterations in collagen fibril arrangement and D-band periodicity, which are seldom detailed in ligament studies. The D-band is a unique ultrastructure in collagen fibrils formed by the periodic arrangement of collagen molecules, playing a critical role in the mechanical properties of fibrils [48]. However, the D-band periodicity lies below the resolution threshold of conventional [49]. To resolve these nanoscale features, AFM was employed, enabling detailed characterization of decellularization-induced modifications in collagen fibrils within ligament tissue. The integrity of the D-period is critically important for the health of collagen fibrils and may influence cell-matrix interactions and tissue biological activity [50]. Its alteration is associated with various pathological conditions and structural changes in tissues [51,52]. The increased D-banding periodicity observed in this study may be associated with partial unwinding of the collagen triple-helix structure or alterations in the molecular packing of collagen fibrils. Guanidine, as a strong chaotropic agent, can induce denaturation of the collagen triple-helix by disrupting hydrogen bonds and hydrophobic interactions, thereby affecting the spatial organization of collagen molecules [53,54]. In addition, the significant removal of GAGs during the decellularization process may disturb the hydration balance between collagen fibrils, leading to local changes in water content and fibrillar swelling, which in turn affects the regularity of D-banding [55]. These findings suggest that collagen structural alterations may result from both direct molecular-level disruption and indirect effects related to matrix organization and hydration state. The documented changes of collagen fibril arrangement and D-band periodicity may critically underlie the compromised mechanical performance of decellularized ligaments, consistent with mechanistic hypotheses previously proposed in tendon and ligament research [27].

The strengths of this study include its comprehensive multiscale analysis of the effects of decellularization. High-resolution AFM was utilized to observe ligament tissue at the nanoscale, enabling the detection of not only structural changes in collagen fibrils but also their nanoscale mechanical properties [56,57]. The use of this advanced imaging technique provided a detailed understanding of collagen fibril behavior. While the study primarily focused on microstructural alterations and their mechanical consequences, modifications in biochemical constituents such as collagen, GAGs, and elastin may also contribute to the observed mechanical changes. Future investigations should aim to delineate these biochemical dynamics to further clarify their roles in post-decellularization tissue behavior.

The results of this study underscore the imperative to refine decellularization protocols to preserve or recover the mechanical integrity of ligament scaffolds while ensuring their biocompatibility. Strategies such as integrating biophysical or biochemical reinforcement methods could enhance the energy dissipation capacity and tensile strength of decellularized scaffolds. Future research should also investigate the functional restoration of the D-band periodicity, which is closely associated with fibrillar organization and mechanical properties. Furthermore, as ligament tissues are subjected to repetitive mechanical loading *in vivo*, fatigue performance represents a critical parameter for evaluating the long-term functionality of scaffolds. While the current study primarily focused on multiscale structural and mechanical alterations induced by decellularization, the absence of cyclic loading assessments remains a limitation. Given the absence of bioreactor platforms capable of precisely replicating physiological mechanical environments, *in vivo* implantation and long-term follow-up may provide a more representative and informative model for assessing scaffold durability and mechanical adaptation. In addition, while this study utilized cells isolated from the bone marrow cavity to evaluate scaffold biocompatibility, no surface marker identification was performed, as the aim was not to assess the stemness or differentiation potential of these cells. This represents a methodological limitation that could be addressed in future studies, particularly if the scaffolds are intended for regenerative applications. Incorporating surface marker analysis, such as flow cytometric or short tandem repeat (STR) profiling for cell authentication, would strengthen the biological relevance and translational potential of the scaffold evaluations.

Conclusions

This investigation comprehensively evaluated the impact of decellularization on the microstructural and mechanical properties of ligament tissues across different scales (micrometer and nanometer). By comparing native and decellularized ligament tissues, we identified microstructural and mechanical changes induced by the decellularization process. The observed reductions in mechanical strength and energy dissipation capacity suggest limited suitability of these scaffolds for immediate application in load-bearing scenarios. Therefore, strategies aimed at restoring mechanical competence are essential to meet the demands of clinical translation. These findings provide valuable insights for the development of advanced scaffold designs that balance structural fidelity with mechanical functionality, thereby advancing their potential for successful *in vivo* deployment.

List of Abbreviations

GAG, glycosaminoglycan; HYP, hydroxyproline; SEM, scanning electron microscopy; F-CHP, fluorescence collagen hybridizing peptide; AFM, atomic force microscopy; HE, hematoxylin-eosin; SD, standard deviation; DNA, deoxyribonucleic acid; RNA, ribonucleic acid; SDS, sodium dodecyl sulfate; DAPI, 4′,6-diamidino-2-phenylindole; DMMB, dimethylmethylene blue; PBS, phosphate buffered saline; EDTA, ethylenediaminetetraacetic acid; PAA, peracetic acid; dECM, decellularized

extracellular matrix; PIP, proximal interphalangeal; CCK-8, Cell Counting Kit-8; ACL, anterior cruciate ligament; LidECM, ligament-derived decellularized extracellular matrix; OCT, optimal cutting temperature.

Availability of Data and Materials

All data reported in this paper will also be shared by the lead contact upon request.

Author Contributions

HZC and NJ contributed to the conception and design of this work and revised critically for important intellectual content. JLS contributed to the acquisition and analysis of data. MYY and JHZ contributed to the interpretation of data. JLS, MYY and JHZ drafted the work and revised critically for important intellectual content. All authors read and approved the final manuscript. All authors agreed to be accountable for all aspects of the work in ensuring that questions related to the accuracy or integrity of any part of the work were appropriately investigated and resolved.

Ethics Approval and Consent to Participate

The research protocol was approved by the Ethics Committee of West China Hospital of Stomatology, Sichuan University (Ethic Approval Number: WCHSIRB-D-2023-469). This study did not involve human participants, and thus, no consent to participate was required.

Acknowledgments

The authors would like to thank Liying Hao (State Key Laboratory of Oral Disease, West China Hospital of Stomatology, Sichuan University) for help in characterizing AFM. The authors thank Zhan Su and Jie Zhang for help in nanoindentation testing and analysis. The graphical abstract was created in BioRender (2025). https://BioRender.com/gkugjua.

Funding

This research was funded by the National Natural Science Foundation of China (No. 82301112), and the Sichuan Science and Technology Program (No. 2024NSFSC1592).

Conflict of Interest

The authors declare no conflict of interest.

Supplementary Material

Supplementary material associated with this article can be found, in the online version, at https://doi.org/10.22203/eCM.v053a03.

References

[1] Nakamichi R, Asahara H. Regulation of tendon and ligament differentiation. Bone. 2021; 143: 115609. https://doi.org/10.1016/j.bone.2020.115609.

[2] Lin J, Shi Y, Men Y, Wang X, Ye J, Zhang C. Mechanical Roles in Formation of Oriented Collagen Fibers. Tissue Engineering. Part B, Reviews. 2020; 26: 116–128. https://doi.org/10.1089/ten.teb.2019.0243.

[3] Asahara H, Inui M, Lotz MK. Tendons and Ligaments: Connecting Developmental Biology to Musculoskeletal Disease Pathogenesis. Journal of Bone and Mineral Research: the Official Journal of the American Society for Bone and Mineral Research. 2017; 32: 1773–1782. https://doi.org/10.1002/jbmr.3199.

[4] Citro V, Clerici M, Boccaccini AR, Della Porta G, Maffulli N, Forsyth NR. Tendon tissue engineering: An overview of biologics to promote tendon healing and repair. Journal of Tissue Engineering. 2023; 14: 20417314231196275. https://doi.org/10.1177/20417314231196275.

[5] Fang J, Wang X, Lai H, Li W, Yao X, Pan Z, *et al*. Decoding the mechanical characteristics of the human anterior cruciate ligament entheses through graduated mineralization interfaces. Nature Communications. 2024; 15: 9253. https://doi.org/10.1038/s41467-024-53542-5.

[6] Wang C, Stovitz SD, Kaufman JS, Steele RJ, Shrier I. Principles of musculoskeletal sport injuries for epidemiologists: a review. Injury Epidemiology. 2024; 11: 21. https://doi.org/10.1186/s40621-024-00507-3.

[7] Martin RL, Davenport TE, Fraser JJ, Sawdon-Bea J, Carcia CR, Carroll LA, *et al*. Ankle Stability and Movement Coordination Impairments: Lateral Ankle Ligament Sprains Revision 2021. The Journal of Orthopaedic and Sports Physical Therapy. 2021; 51: CPG1–CPG80. https://doi.org/10.2519/jospt.2021.0302.

[8] Aicale R, Tarantino D, Maffulli N. Overuse injuries in sport: a comprehensive overview. Journal of Orthopaedic Surgery and Research. 2018; 13: 309. https://doi.org/10.1186/s13018-018-1017-5.

[9] Romero-Morales C, López-López D, Almazán-Polo J, Mogedano-Cruz S, Sosa-Reina MD, García-Pérez-de-Sevilla G, *et al*. Prevalence, diagnosis and management of musculoskeletal disorders in elite athletes: A mini-review. Disease-a-Month: DM. 2024; 70: 101629. https://doi.org/10.1016/j.disamonth.2023.101629.

[10] Garriga C, Goff M, Paterson E, Hrusecka R, Hamid B, Alderson J, *et al*. Clinical and molecular associations with outcomes at 2 years after acute knee injury: a longitudinal study in the Knee Injury Cohort at the Kennedy (KICK). The Lancet. Rheumatology. 2021; 3: e648–e658. https://doi.org/10.1016/S2665-9913(21)00116-8.

[11] Svantesson E, Hamrin Senorski E, Webster KE, Karlsson J, Diermeier T, Rothrauff BB, *et al*. Clinical outcomes after anterior cruciate ligament injury: panther symposium ACL injury clinical outcomes consensus group. Knee Surgery, Sports Traumatology, Arthroscopy: Official Journal of the ESSKA. 2020; 28: 2415–2434. https://doi.org/10.1007/s00167-020-06061-x.

[12] Filbay SR, Dowsett M, Chaker Jomaa M, Rooney J, Sabharwal R, Lucas P, *et al*. Healing of acute anterior cruciate ligament rupture on MRI and outcomes following non-surgical management with the Cross Bracing Protocol. British Journal of Sports Medicine. 2023; 57: 1490–1497. https://doi.org/10.1136/bjsports-2023-106931.

[13] Ruiz-Alonso S, Lafuente-Merchan M, Ciriza J, Saenz-Del-Burgo L, Pedraz JL. Tendon tissue engineering: Cells, growth factors, scaffolds and production techniques. Journal of Controlled Release: Official Journal of the Controlled Release Society. 2021; 333: 448–486. https://doi.org/10.1016/j.jconrel.2021.03.040.

[14] Ning C, Li P, Gao C, Fu L, Liao Z, Tian G, *et al*. Recent advances in tendon tissue engineering strategy. Frontiers in Bioengineering and Biotechnology. 2023; 11: 1115312. https://doi.org/10.3389/fbioe.2023.1115312.

[15] Leong NL, Kator JL, Clemens TL, James A, Enamoto-Iwamoto M, Jiang J. Tendon and Ligament Healing and Current Approaches to Tendon and Ligament Regeneration. Journal of Orthopaedic Research: Official Publication of the Orthopaedic Research Society. 2020; 38: 7–12. https://doi.org/10.1002/jor.24475.

[16] Anjum S, Li T, Saeed M, Ao Q. Exploring polysaccharide and protein-enriched decellularized matrix scaffolds for tendon and ligament repair: A review. International Journal of Biological Macromolecules. 2024; 254: 127891. https://doi.org/10.1016/j.ijbiomac.2023.127891.

[17] Golebiowska AA, Intravaia JT, Sathe VM, Kumbar SG, Nukavarapu SP. Decellularized extracellular matrix biomaterials for regenerative therapies: Advances, challenges and clinical prospects. Bioactive Materials. 2024; 32: 98–123. https://doi.org/10.1016/j.bioactmat.2023.09.017.

[18] Xu P, Kankala RK, Wang S, Chen A. Decellularized extracellular matrix-based composite scaffolds for tissue engineering and regenerative medicine. Regenerative Biomaterials. 2023; 11: rbad107. https://doi.org/10.1093/rb/rbad107.

[19] Gadre M, Kasturi M, Agarwal P, Vasanthan KS. Decellularization and Their Significance for Tissue Regeneration in the Era of 3D Bioprinting. ACS Omega. 2024; 9: 7375–7392. https://doi.org/10.1021/acsomega.3c08930.

[20] Brouki Milan P, Masoumi F, Biazar E, Zare Jalise S, Mehrabi A. Exploiting the Potential of Decellularized Extracellular Matrix (ECM) in Tissue Engineering: A Review Study. Macromolecular Bioscience. 2025; 25: e2400322. https://doi.org/10.1002/mabi.202400322.

[21] Liu J, Song Q, Yin W, Li C, An N, Le Y, *et al*. Bioactive scaffolds for tissue engineering: A review of decellularized extracellular matrix applications and innovations. Exploration. 2024; 5: 20230078. https://doi.org/10.1002/EXP.20230078.

[22] Moffat D, Ye K, Jin S. Decellularization for the retention of tissue niches. Journal of Tissue Engineering. 2022; 13: 20417314221101151. https://doi.org/10.1177/20417314221101151.

[23] Behmer Hansen RA, Wang X, Kaw G, Pierre V, Senyo SE. Accounting for Material Changes in Decellularized Tissue with Underutilized Methodologies. BioMed Research International. 2021; 2021: 6696295. https://doi.org/10.1155/2021/6696295.

[24] Jiang N, Chen H, Zhang J, Cao P, Wang P, Hou Y, *et al*. Decellularized-disc based allograft and xenograft prosthesis for the long-term precise reconstruction of temporomandibular joint disc. Acta Biomaterialia. 2023; 159: 173–187. https://doi.org/10.1016/j.actbio.2023.01.042.

[25] Endress R, Woon CY, Farnebo SJ, Behn A, Bronstein J, Pham H, *et al*. Tissue-engineered collateral ligament composite allografts for scapholunate ligament reconstruction: an experimental study. The Journal of Hand Surgery. 2012; 37: 1529–1537. https://doi.org/10.1016/j.jhsa.2012.05.020.

[26] Zhou SY, Yuan B, Huang WM, Chen XS, Jia LS. Aponeurosis discission, a low-detergent method for tissue-engineered acellular ligament scaffolds. Journal of Materials Science. Materials in Medicine. 2022; 33: 40. https://doi.org/10.1007/s10856-022-06661-8.

[27] Uquillas JA, Spierings J, van der Lande A, Eren AD, Bertrand M, Yuan H, *et al*. An off-the-shelf decellularized and sterilized human bone-ACL-bone allograft for anterior cruciate ligament reconstruction. Journal of the Mechanical Behavior of Biomedical Materials. 2022; 135: 105452. https://doi.org/10.1016/j.jmbbm.2022.105452.

[28] Chae S, Choi YJ, Cho DW. Mechanically and biologically promoted cell-laden constructs generated using tissue-specific bioinks for tendon/ligament tissue engineering applications. Biofabrication. 2022; 14. https://doi.org/10.1088/1758-5090/ac4fb6.

[29] Li Y, Zhu T, Wang L, Jiang J, Xie G, Huangfu X, *et al*. Tissue-Engineered Decellularized Allografts for Anterior Cruciate Ligament Reconstruction. ACS Biomaterials Science & Engineering. 2020; 6: 5700–5710. https://doi.org/10.1021/acsbiomaterials.0c00269.

[30] Xu K, Kuntz LA, Foehr P, Kuempel K, Wagner A, Tuebel J, *et al*. Efficient decellularization for tissue engineering of the tendon-bone interface with preservation of biomechanics. PloS One. 2017; 12: e0171577. https://doi.org/10.1371/journal.pone.0171577.

[31] de Lima Santos A, da Silva CG, de Sá Barreto LS, Leite KRM, Tamaoki MJS, Ferreira LM, *et al*. A new decellularized tendon scaffold for rotator cuff tears—evaluation in rabbits. BMC Musculoskeletal Disorders. 2020; 21: 689. https://doi.org/10.1186/s12891-020-03680-w.

[32] Zhao J, Meng F, Qian J, Huang Y, Fan Y. *In vitro* cell stretching devices and their applications: From cardiomyogenic differentiation to tissue engineering. Medicine in Novel Technology and Devices. 2023; 18: 100220. https://doi.org/10.1016/j.medntd.2023.100220.

[33] Rashid B, Destrade M, Gilchrist MD. Mechanical characterization of brain tissue in tension at dynamic strain rates. Journal of the Mechanical Behavior of Biomedical Materials. 2014; 33: 43–54. https://doi.org/10.1016/j.jmbbm.2012.07.015.

[34] Morejon A, Mantero AMA, Best TM, Jackson AR, Travascio F. Mechanisms of energy dissipation and relationship with tissue composition in human meniscus. Osteoarthritis and Cartilage/OARS, Osteoarthritis Research Society. 2022; 30: 605–612. https://doi.org/10.1016/j.joca.2022.01.001.

[35] Luo C, Chung C, Traugutt NA, Yakacki CM, Long KN, Yu K. 3D Printing of Liquid Crystal Elastomer Foams for Enhanced Energy Dissipation Under Mechanical Insult. ACS Applied Materials & Interfaces. 2021; 13: 12698–12708. https://doi.org/10.1021/acsami.0c17538.

[36] Sehic E, de Miguel-Gómez L. Standardizing decellularization protocols for optimized uterine tissue bioengineering. Regenerative Therapy. 2024; 28: 183–190. https://doi.org/10.1016/j.reth.2024.12.011.

[37] Seyler TM, Bracey DN, Plate JF, Lively MO, Mannava S, Smith TL, *et al*. The Development of a Xenograft-Derived Scaffold for Tendon and Ligament Reconstruction Using a Decellularization and Oxidation Protocol. Arthroscopy: the Journal of Arthroscopic & Related Surgery: Official Publication of the Arthroscopy Association of North America and the International Arthroscopy Association. 2017; 33: 374–386. https://doi.org/10.1016/j.arthro.2016.07.016.

[38] Zhang J, Xie L, She Y, Luo H, Zhu S, Jiang N. Microstructural and Micromechanical Properties of Decellularized Fibrocartilaginous Scaffold. ACS Biomaterials Science & Engineering. 2025; 11: 1562–1570. https://doi.org/10.1021/acsbiomaterials.4c01195.

[39] Arakawa T, Niikura T, Kita Y, Akuta T. Sodium Dodecyl Sulfate Analogs as a Potential Molecular Biology Reagent. Current Issues in Molecular Biology. 2024; 46: 621–633. https://doi.org/10.3390/cimb46010040.

[40] Kim YS, Majid M, Melchiorri AJ, Mikos AG. Applications of decellularized extracellular matrix in bone and cartilage tissue engineering. Bioengineering & Translational Medicine. 2018; 4: 83–95. https://doi.org/10.1002/btm2.10110.

[41] Zitnay JL, Li Y, Qin Z, San BH, Depalle B, Reese SP, *et al*. Molecular level detection and localization of mechanical damage in collagen enabled by collagen hybridizing peptides. Nature Communications. 2017; 8: 14913. https://doi.org/10.1038/ncomms14913.

[42] Li X, Zhang Q, Yu SM, Li Y. The Chemistry and Biology of Collagen Hybridization. Journal of the American Chemical Society. 2023; 145: 10901–10916. https://doi.org/10.1021/jacs.3c00713.

[43] Tao P, Liu J, Li Y, Zhang T, Wang F, Chang L, *et al*. Damaged collagen detected by collagen hybridizing peptide as efficient diagnosis marker for early hepatic fibrosis. Biochimica et Biophysica Acta. Gene Regulatory Mechanisms. 2023; 1866: 194928. https://doi.org/10.1016/j.bbagrm.2023.194928.

[44] Seelemann CA, Willett TL. Empirical evidence that bone collagen molecules denature as a result of bone fracture. Journal of the Mechanical Behavior of Biomedical Materials. 2022; 131: 105220. https://doi.org/10.1016/j.jmbbm.2022.105220.

[45] Kiener D, Wurmshuber M, Alfreider M, Schaffar GJK, Maier-Kiener V. Recent advances in nanomechanical and *in situ* testing techniques: Towards extreme conditions. Current Opinion in Solid State and Materials Science. 2023; 27: 101108. https://doi.org/10.1016/j.cossms.2023.101108.

[46] Enrriques AE, Howard S, Timsina R, Khadka NK, Hoover AN, Ray AE, *et al*. Atomic Force Microscopy Cantilever-Based Nanoindentation: Mechanical Property Measurements at the Nanoscale in Air and Fluid. Journal of Visualized Experiments: JoVE. 2022; 190: 10.3791/64497. https://doi.org/10.3791/64497.

[47] Balestrini JL, Gard AL, Liu A, Leiby KL, Schwan J, Kunkemoeller B, *et al*. Production of decellularized porcine lung scaffolds for use in tissue engineering. Integrative Biology: Quantitative Biosciences from Nano to Macro. 2015; 7: 1598–1610. https://doi.org/10.1039/c5ib00063g.

[48] Darvish DM. Collagen fibril formation *in vitro*: From origin to opportunities. Materials Today. Bio. 2022; 15: 100322. https://doi.org/10.1016/j.mtbio.2022.100322.

[49] Stylianou A. Assessing Collagen D-Band Periodicity with Atomic Force Microscopy. Materials. 2022; 15: 1608. https://doi.org/10.3390/ma15041608.

[50] Sweeney SM, Orgel JP, Fertala A, McAuliffe JD, Turner KR, Di Lullo GA, *et al*. Candidate cell and matrix interaction domains on the collagen fibril, the predominant protein of vertebrates. The Journal of Biological Chemistry. 2008; 283: 21187–21197. https://doi.org/10.1074/jbc.M709319200.

[51] Leighton MP, Rutenberg AD, Kreplak L. D-band strain underestimates fibril strain for twisted collagen fibrils at low strains. Journal of the Mechanical Behavior of Biomedical Materials. 2021; 124: 104854. https://doi.org/10.1016/j.jmbbm.2021.104854.

[52] Zhou B, Tu T, Gao Z, Wu X, Wang W, Liu W. Impaired collagen fibril assembly in keloids with enhanced expression of lumican and collagen V. Archives of Biochemistry and Biophysics. 2021; 697: 108676. https://doi.org/10.1016/j.abb.2020.108676.

[53] Elsaesser AF, Bermueller C, Schwarz S, Koerber L, Breiter R, Rotter N. *In vitro* cytotoxicity and *in vivo* effects of a decellularized xenogeneic collagen scaffold in nasal cartilage repair. Tissue Engineering. Part A. 2014; 20: 1668–1678. https://doi.org/10.1089/ten.TEA.2013.0365.

[54] Zhang Q, Li X, Huang K, Huang Y, Zhao S, Liu S, *et al*. Controlling the Trimerization of the Collagen Triple-Helix by Solvent Switching. Biomacromolecules. 2023; 24: 1689–1699. https://doi.org/10.1021/acs.biomac.2c01475.

[55] Bera AK, Sriya Y, Pati F. Formulation of Dermal Tissue Matrix Bioink by a Facile Decellularization Method and Process Optimization for 3D Bioprinting toward Translation Research. Macromolecular Bioscience. 2022; 22: e2200109. https://doi.org/10.1002/mabi.202200109.

[56] Stylianou A, Kontomaris SV, Grant C, Alexandratou E. Atomic Force Microscopy on Biological Materials Related to Pathological Conditions. Scanning. 2019; 2019: 8452851. https://doi.org/10.1155/2019/8452851.

[57] Zhou Y, Du J. Atomic force microscopy (AFM) and its applications to bone-related research. Progress in Biophysics and Molecular Biology. 2022; 176: 52–66. https://doi.org/10.1016/j.pbiomolbio.2022.10.002.

Editor's note: The Scientific Editor responsible for this paper was Kaili Lin.

Received: 11th January 2025; **Accepted**: 16th June 2025; **Published**: 30th September 2025